JOURNAL OF SYNCHROTRON RADIATION
ISSN 1600-5775

Growth of block copolymer stabilized metal nanoparticles probed simultaneously by *in situ* XAS and UV–Vis spectroscopy

C. Nayak,[a,b] D. Bhattacharyya,[a,b]* S. N. Jha[a,b] and N. K. Sahoo[a,b]

[a]Bhabha Atomic Research Centre, Mumbai 400 085, India, and [b]Homi Bhabha National Institute, Mumbai 400 094, India. *Correspondence e-mail: dibyendubarc@gmail.com

Received 28 July 2015
Accepted 19 November 2015

Edited by A. F. Craievich, University of São Paulo, Brazil

Keywords: dispersive XAS; *in situ*; nanoparticle; UV–Vis.

The growth of Au and Pt nanoparticles from their respective chloride precursors using block copolymer-based reducers has been studied by simultaneous *in situ* measurement of XAS and UV–Vis spectroscopy at the energy-dispersive EXAFS beamline (BL-08) at INDUS-2 SRS at RRCAT, Indore, India. While the XANES spectra of the precursor give real-time information on the reduction process, the EXAFS spectra reveal the structure of the clusters formed at the intermediate stages of growth. The growth kinetics of both types of nanoparticles are found to be almost similar and are found to follow three stages, though the first stage of nucleation takes place earlier in the case of Au than in the case of Pt nanoparticles due to the difference in the reduction potential of the respective precursors. The first two stages of the growth of Au and Pt nanoparticles as obtained by *in situ* XAS measurements could be corroborated by simultaneous *in situ* measurement of UV–Vis spectroscopy also.

1. Introduction

Noble metal nanoparticles are important due to their unique properties and wide variety of applications in different fields, among which gold and platinum seek special attention. They have applications in biotechnology, catalysis and optoelectronics (Storhoff *et al.*, 1998; Bond *et al.*, 2006; Tsung *et al.*, 2009; Narayanan & El-Sayed, 2004; Louis & Pluchery, 2012; Schmid, 2006). The properties of these nanoparticles are highly dependent on their size and shape, thus accentuating the importance of their synthesis process.

Although gold and platinum nanoparticles are one of the widely studied nano-systems and have been subjected to various studies, the initial stages of nucleation and growth of these nanoparticles have remained unexplored for a long time. This is mainly due to the scarcity of suitable experimental techniques for exploring the initial stages of growth. Techniques like UV–Vis spectroscopy (Hu *et al.*, 2005; Wong *et al.*, 1998) are quite popular for studying the kinetics of formation of nanoparticles from the solution phase, though they are limited to systems which absorb in this particular wavelength range. Transmission electron microscopy (TEM) (Zheng *et al.*, 2009; Simonsen *et al.*, 2010) is another popular technique for studying the changes in particle size; however, in this case the electron beam can interfere with the reacting species thus changing the whole redox reaction process to be studied and it is also difficult to be employed *in situ* in solution phase due to vacuum requirements. X-ray-based techniques, on the other hand, are not generally system specific and in most cases do not alter the process to be studied. With the advent of synchrotron-based techniques, many X-ray-based experiments

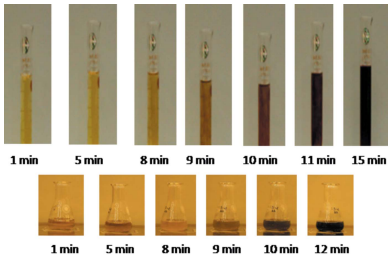

are being carried out to investigate the growth of nanoparticles; for example, small-angle X-ray scattering (SAXS) is one of the important methods among these (Abécassis *et al.*, 2007; Wang *et al.*, 2008; Caetano *et al.*, 2011; Polte *et al.*, 2010). However, all the above techniques mostly yield information on real-time changes in particle size only and cannot throw light on the evolution of the reduction process that is mainly responsible for the nucleation and growth of nanoparticles in such systems. Also, using these techniques we cannot find out the coordination of atoms in clusters which are formed in the initial phase of the growth and act as seeds for further growth of the nanoparticles.

Time-resolved X-ray absorption spectroscopy (XAS), which includes both X-ray near-edge structure (XANES) and extended X-ray absorption fine-structure (EXAFS) techniques, on the other hand, can simultaneously give insight into the structural changes in the species during growth of nanoparticles as well as in the oxidation states of the metal cations. Recently several *in situ* time-resolved EXAFS measurements have been carried out on gold and platinum nanoparticles synthesized by various routes *viz* the Turkevich method by Polte *et al.* (2010) and Lin *et al.* (2006), the Shiffrin–Brust method by Ohyama *et al.* (2011), X-ray irradiation of ionic liquid by Ma *et al.* (2013), photoreduction by Harada & Kamigaito (2012), polyol synthesis by Boita *et al.* (2014) *etc*. Through these experiments the understanding of these processes has been improved, which has ultimately helped to obtain a better yield and distribution of the nanoparticles. Often several other complementary techniques have also been used with time-resolved EXAFS for simultaneous measurements to gain a better insight into the reaction procedure. For example, Shannon *et al.* (1997) combined XAFS with X-ray diffraction to study solid–liquid catalytic reactions to obtain information on short-range and long-range structural changes. Tromp *et al.* (2003) carried out XAFS and UV–Vis spectroscopy simultaneously. Bauer *et al.* (2010) have carried out simultaneous *in situ* measurements of UV–Vis spectroscopy and XANES to study the reduction of Ce (+4) to Ce (+3). Raman, UV–Vis and XANES have been used simultaneously by Briois *et al.* (2005), a three-dimensional *in situ* set up for simultaneous measurements of Raman, UV–Vis and XAS to study homogeneous catalysis has been proposed by Bauer & Gastl (2010), while *in situ* XAFS, IR and mass spectroscopy have been combined for heterogeneous catalysis studies by Newton *et al.* (2004). Complementary techniques give a broader view of the system and focus on different aspects of it which in turn results in more consolidated conclusions.

In the present study we have combined EXAFS and UV–Vis spectroscopy to study the growth of gold and platinum nanoparticles stabilized by block copolymer. Block copolymers consist of two or more chemically distinct polymeric units connected by covalent or non-covalent bonds. Block copolymer forms a crown ether structure which engulfs metal ions and acts as both reducing and stabilizing agents. Sodium citrate and ascorbic acid are used as additional reducing agents in this reaction. This method gives a high yield of nanoparticles as suggested by Ray *et al.* (2011) for gold nanoparticles. According to their findings, the concentration and size of nanoparticles increase to some extent only by increasing the concentration of Au precursor, since there is a 1:1 involvement of the precursor and the reducer in the growth process and maximum concentration of nanoparticles is obtained when the concentrations of the precursor and reducer are the same. However, due to the measurement limitations of the small-angle neutron scattering technique, the authors could not investigate the structural changes during growth of nanoparticles. Therefore, in the present study we have taken the optimized concentrations of the precursor and the reducer as suggested by Ray *et al.* (2011) and focused on the structural evolution during the growth of nanoparticles by block copolymer mediated synthesis using time-resolved EXAFS. To the best of our knowledge this is the first time that *in situ* EXAFS measurements on block copolymer mediated synthesis processes have been reported.

2. Experimental details

2.1. Synthesis of nanoparticles

Gold nanoparticles have been synthesized by mixing 2.5 ml of 60 m*M* chloroauric acid ($HAuCl_4.3H_2O$) with 1.5 ml of 100 m*M* trisodium citrate (Na_3Ct) and 1 ml of 10 m*M* P85 block copolymer. The solution is kept undisturbed at room temperature. After ∼10 min the colour of the solution starts changing to red and after ∼15 min becomes dark violet, as shown in Fig. 1(*a*), manifesting the formation of Au nanoparticles. The concentration of gold in the final solution is 30 m*M*. Platinum nanoparticles were synthesized by mixing 2.5 ml of 60 m*M* chloroplatinic acid ($H_2PtCl_6.6H_2O$) with 2.5 ml of 500 m*M* ascorbic acid and 1 ml of 10 m*M* P85 block copolymer and by heating the mixture to 50°C. The solution first becomes colourless and in 12 min changes to brown and

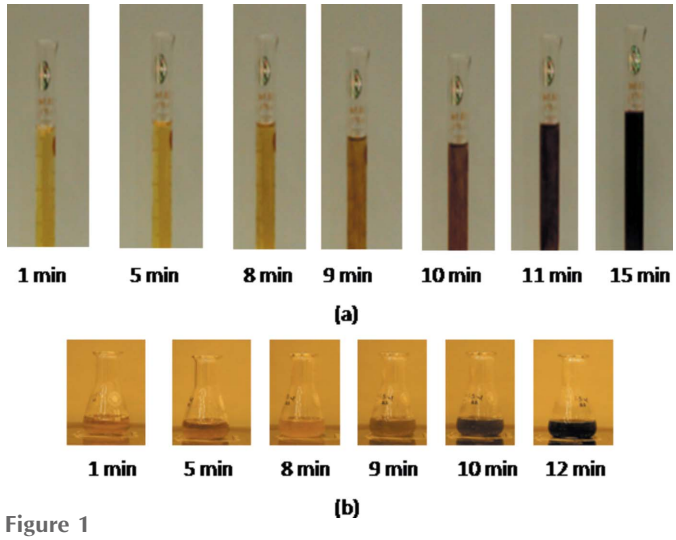

Figure 1
(*a*) Changes in colour of the Au nanoparticle precursor solution with time after mixing the reducers. (*b*) Changes in colour of the Pt nanoparticle precursor solution with time after mixing the reducers.

then to black as shown in Fig. 1(*b*), showing the formation of Pt nanoparticles.

For the present study, the above synthesis process has been carried out in a specially designed Teflon reaction cell having paths for both X-rays and UV–Vis radiation in mutually perpendicular directions. X-rays are transmitted through Kapton windows while the optical light is passed using optical fibres which are capped with Teflon ferrules and are directly immersed into the solution. The cell has been designed and fabricated in such a way that the optical paths can vary from 5 mm to 20 mm for X-rays and from 2 mm to 20 mm for UV–Vis radiation. The volume of the cell varies according to the adjustment of the Kapton windows and optical fibres. However, for the present experiment, where Kapton windows are adjusted to be 10 mm apart and the Teflon ferrules are adjusted such that optical fibres are positioned 5 mm apart, the volume of the cell is approximately 8 ml. The sample mount of the beamline has been modified so that the *in situ* reaction cell can be placed on a magnetic stirrer-cum-heater for mixing and heating the reaction solution. The precursor is taken in the Teflon reaction cell and the respective reducer is injected into it through a Teflon tube using a computer-controlled motor-driven syringe pump. The reducer is injected at a speed of 5 ml min^{-1} and the reaction solution is stirred with a speed of about 60 rpm to have a homogeneous solution. As has been mentioned above, for synthesis of Au nanoparticles the reaction solution remains at room temperature while in the case of the formation of Pt nanoparticles the solution is heated to 50°C. The experimental setup for simultaneous time-resolved EXAFS measurement and UV–Vis absorption measurement is shown in Fig. 2.

2.2. Characterization

In the present study the growth of nanoparticles has been carried out by taking the chloride precursors in the Teflon reaction cell described above and, as the reaction proceeds, *in situ* XAS and UV–Vis spectroscopy measurements have been carried out at regular time intervals starting from the instant of adding the reducers to the respective precursors.

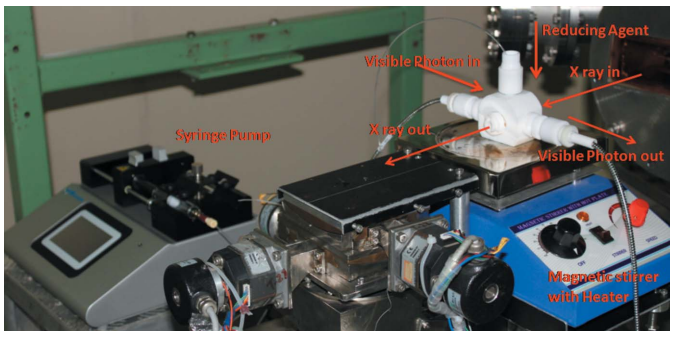

Figure 2
Photograph of the Teflon reaction cell at the sample position of the energy-dispersive EXAFS beamline (BL-08) for *in situ* XAFS and UV–Vis spectroscopy measurements.

Time-resolved EXAFS measurement has been carried out at the energy-dispersive EXAFS beamline (BL-8) at the INDUS-2 synchrotron source (2.5 GeV, 100 mA) at the Raja Ramanna Centre for Advanced Technology (RRCAT), Indore, India (Bhattacharyya *et al.*, 2009). The above beamline uses a 460 mm-long Si (111) crystal mounted on a mechanical crystal bender which can bend the crystal to the shape of an ellipse (Das *et al.*, 2004). The crystal selects a particular band of energy from white synchrotron radiation depending on the grazing angle of incidence of the synchrotron beam (Bragg angle) and disperses as well as focuses the band on the sample. The transmitted radiation from the sample diverges further and is detected by a position-sensitive detector (PSD). A plot of absorption *versus* photon energy is obtained by recording the intensities I_0 and I_t on the PSD, without and with the sample, respectively, and using the relation, $I_t = I_0 \exp(-\mu t)$ where μ is the absorption coefficient and t is the thickness of the absorber. Thus the whole absorption spectrum can be recorded simultaneously on the detector within a fraction of a second. For *in situ* XAS measurements the Teflon reaction cell has been placed at the sample position and the Kapton windows of the cell were adjusted to obtain an optical path length of 10 mm for X-rays through the solution.

For XAS measurement at the Au L_3-edge the radiation transmitted through the sample is detected by a position-sensitive CCD detector which is a 25 mm × 25 mm detector with 2048 × 2048 pixels, each of 13.5 µm × 13.5 µm size. For each spectrum 100 scans have been accumulated to improve the signal-to-noise ratio and XAS spectra have been recorded every minute for 2 h. However, for XAS measurement at the Pt L_3-edge the radiation transmitted through the sample is detected by a position-sensitive Mythen detector (M/s, Dectris, Switzerland). The Mythen detector is a one-dimensional X-ray detector containing 1280 silicon microstrips. It operates in single-photon-counting mode thus leading to no readout noise. For each spectrum the exposure time has been fixed to 1 min to improve the signal-to-noise ratio and XAS spectra have been recorded every minute for 2 h. The beamline configuration is adjusted so that a spreading of the energy band at a rate of ∼1 eV $pixel^{-1}$ is achieved on the CCD and the Mythen detectors at photon energies corresponding to the Au and Pt L_3-edges, respectively.

It should be noted that the life time of the stored beam in the INDUS-2 storage ring is more than 24 h at a beam current of 75 mA at which the above EXAFS data were recorded. Hence the beam current and the incident photon flux have not decreased by any significant amount during the span of data acquisition. This has been ensured by measuring the I_0 spectra at the beginning and end of each set of experiments.

UV–Vis absorption measurements have been been carried out simultaneously with the XAS measurements using an optical fibre based spectrometer (M/s, Avantes, Netherlands) where the optical fibre tips are capped with Teflon ferrules and are directly immersed into the solution. Light from the source is transmitted to the solution through optical fibre and is collected by another optical fibre to the spectrometer. The

path of the beam inside the liquid is 5 mm. UV–Vis spectra have been collected at an interval of 1 min for 30 min.

Ex situ TEM images of the nanoparticles were collected using a CM200 machine with tungsten filament operated at an acceleration voltage of 200 kV with a resolution of 2.4 Å. Metal nanoparticles, after 90 min of reaction, have been collected, washed, centrifuged and then re-dispersed in water by ultrasonicating for 20 min. A drop of this solution was placed on a copper grid, dried at room temperature and then imaged by TEM.

3. Results and discussions

3.1. Growth of gold nanoparticles

Fig. 3 shows *in situ* time-resolved XANES spectra of the gold precursor reaction solution measured at the Au L_3-edge. It can be seen that the near-edge spectrum of $HAuCl_4$ shows a white line at 11923 eV which is due to electronic transition from the $2p_{3/2}$ to $5d$ state. This white line is a characteristic of Au^{+3} and disappears for metallic Au due to fully filled $5d$ states. The decrease in the intensity of the white line and finally its disappearance with time suggests reduction of $HAuCl_4$ and formation of metallic gold nanoparticles. After 90 min from the start of the reaction the spectrum fully resembles that of a metallic gold spectrum.

As has been mentioned by Helmbrecht *et al.* (2015), the Au L_3-edge data do not show a linear shift with change in oxidation state of Au due to the overlapping of the $2p$–$5d$ transition peak with the edge. Thus a linear combination fit of the time-resolved XANES spectra was performed considering $HAuCl_4$ and Au foil spectra as standards of the +3 and +0 states to obtain a quantitative measure of the presence of the two species in the reaction solution at a particular reaction time. From the linear combination fit of the time-resolved XANES spectra it has been observed that after 10 min about 50% of the Au cations are in the metallic (+0) state and after 90 min about 87% of the Au cations are reduced to the +0 state. A similar approach has been followed by others (Ohyama *et al.*, 2011; Polte *et al.*, 2010; Boita *et al.*, 2014) for *in situ* observation of nucleation and growth of Au and Pt nanoparticles from solution phases using XANES measurement.

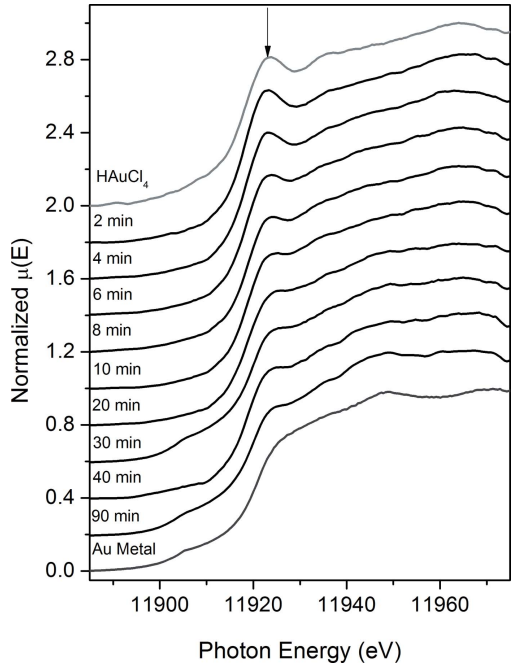

Figure 3
XANES spectra of Au nanoparticle precursor solution measured at the Au L_3-edge at different time intervals after mixing the reducers.

It should be noted here that in the present case distinct features in the XANES spectra due to the presence of different Au clusters (Au_{12}, Au_{13} and Au_{147}), which have been predicted from EXAFS results (discussed later), could not be seen. The XANES spectra of Au_{13} clusters have been reported by Menard *et al.* (2006) where they have also found that the XANES features are similar to that of Au foil with higher white-line intensity. Tsunoyama *et al.* (2009), while studying PVP and PPA stabilized Au clusters of various sizes in the range 1–4 nm, have also found that the effect of size only appears in the white-line intensity of XANES spectra, due to the change in density of d holes available mainly for $2p_{3/2}$ to $5d_{5/2}$ transitions. However, the above studies deal with XANES measurements on a particular cluster system formed by a particular experimental route. Since, in our study, multiple phases are present at a particular reaction time and the XANES spectrum of the Au_{13} cluster itself resembles that of Au foil, it is not possible to identify the signatures of still larger clusters from the Au L_3-edge XANES spectra.

It can be seen from Fig. 3 that a pre-edge-like feature appears at ∼11905 eV for a few cases where larger nanoparticles are expected to be grown and also for the Au metal foil. The origin of this feature is still not fully understood. The fact that it also appears in the case of Au foil, and it does not appear in the case of Pt nanoparticles, as can be seen from Fig. 9, excludes the possibility of its origin due to small-angle scattering by the formed nanoparticles. Also, the fact that it does not appear in all stages of the Au nanoparticles growth also proves that it is not a beamline artefact. We will carry out additional experiments to clarify this. Presently we have not attempted to give any definite explanation for this and this feature does not affect the overall results and conclusion of the present manuscript.

In order to analyse the EXAFS spectra of the samples, the absorption coefficient $\mu(E)$ has been converted to the absorption function $\chi(E)$ defined as follows (Konigsberger & Prins, 1988):

$$\chi(E) = \frac{\mu(E) - \mu_0(E)}{\Delta\mu_0(E_0)}, \qquad (1)$$

where E_0 is the absorption edge energy, $\mu_0(E_0)$ is the bare atom background and $\Delta\mu_0(E_0)$ is the step in the $\mu(E)$ value at the absorption edge. After converting the energy scale to the photoelectron wavenumber scale (k), as defined by

$$k = \left[\frac{2m(E - E_0)}{\hbar^2}\right]^{1/2}, \quad (2)$$

the energy-dependent absorption coefficient $\chi(E)$ has been converted to the wavenumber-dependent absorption coefficient $\chi(k)$, where m is the electron mass. Finally, $\chi(k)$ is weighted by k^2 to amplify the oscillation at high k. The functions $\chi(k)k^2$ are Fourier transformed (FT) in r-space to generate the $\chi(r)$ *versus* r (or FT-EXAFS) spectra in terms of the distances from the centre of the absorbing atom. However, it should be noted here that, in the $\chi(r)$ *versus* r plots, r does not represent the real distance from the centre of the absorbing atom, because of the phase-shift suffered by the photoelectron wave during scattering, and the real distance is obtained by fitting the experimentally derived data with those theoretically generated. It should be mentioned here that a set of EXAFS data analysis programs available within the *IFEFFIT* software package (Newville, 2001) have been used for reduction and fitting of the experimental EXAFS data. This includes data reduction and Fourier transform to derive the $\chi(r)$ *versus* r spectra from the absorption spectra, generation of the theoretical EXAFS spectra starting from an assumed crystallographic structure, and finally fitting of the experimental data with the theoretical spectra using the *FEFF 6.0* code. The goodness of fit has been determined by the value of $R_{\rm factor}$, defined by

$$R_{\rm factor} = \sum \frac{\{{\rm Im}[\chi_{\rm dat}(r_i) - \chi_{\rm th}(r_i)]\}^2 + \{{\rm Re}[\chi_{\rm dat}(r_i) - \chi_{\rm th}(r_i)]\}^2}{\{{\rm Im}[\chi_{\rm dat}(r_i)]\}^2 + \{{\rm Re}[\chi_{\rm dat}(r_i)]\}^2} \quad (3)$$

where $\chi_{\rm dat}$ and $\chi_{\rm th}$ refer to the experimental and theoretical $\chi(r)$ values, respectively, and Im and Re refer to the imaginary and real parts of the respective quantities.

Fig. 4 shows the $\chi(r)$ *versus* r spectra taken at different intervals of time during the growth of gold nanoparticles. The k range used for the Fourier transform is 3–9.5 Å^{-1}. The first peak (~1.8 Å) corresponds to the Au—Cl bond and the second peak (~2.6 Å) corresponds to the Au—Au bond. The $\chi(r)$ *versus* r spectra have been fitted assuming an Au—Cl path and an Au—Au path. The $R_{\rm factor}$ values of all fits are less than 0.01 which ensures a good fit. The values of the Debye–Waller factors (σ^2) have been kept fixed at 0.002 and 0.001 for the Au—Cl and Au—Au bonds, respectively, which have been found by fitting the data of the Au precursor (having only Au—Cl bonds) and Au nanoparticles formed after 90 min of reaction (having only Au—Au bonds), respectively. The values of the Debye–Waller factors are kept constant to reduce the number of parameters during fitting and to obtain a more reliable fit. Similarly, ΔE_0 values obtained from the fitting of the EXAFS data of the precursor and the end products (0 min and 90 min data, respectively) are used for the two paths and kept constant during fitting.

In the case of EXAFS fitting, the maximum number of independent points is generally given by the Nyquist criteria $N_{\rm ind} = 2\Delta k \Delta r/\pi$. In this case, $\Delta k = 9.5 - 3 = 6.5$ and $\Delta r = 3 - 1 = 2$, yielding $N_{\rm ind} = 8.3$. Since the Debye–Waller factors and ΔE_0 values of the various paths are kept constant, only four parameters are varied (bond distance and coordination number for two paths) during the fitting which is much less than the maximum number of independent points. A similar approach has also been taken by other researchers while analysing EXAFS data of nanoparticles. For example, Ma *et al.* (2013) in their study of X-ray induced formation of gold nanoparticles have varied only the coordination number and bond lengths and kept the Debye–Waller factor constant while fitting the EXAFS data. Similarly, Yao *et al.* (2012), while studying the formation mechanism of Rh nanocubes by *in situ* dispersive EXAFS measurements, have also kept the Debye–Waller factor fixed. Harada & Kamigaito (2012) have also found that the Debye–Waller factor for the Pt—Pt bond, in the case of the growth of Pt nanoparticles, does not show any time dependence and is close to that of bulk Pt. The experimental $\chi(r)$ *versus* r data for some of the representative reaction times, along with their best fit theoretical plots carried out as discussed above, are shown in Fig. 5.

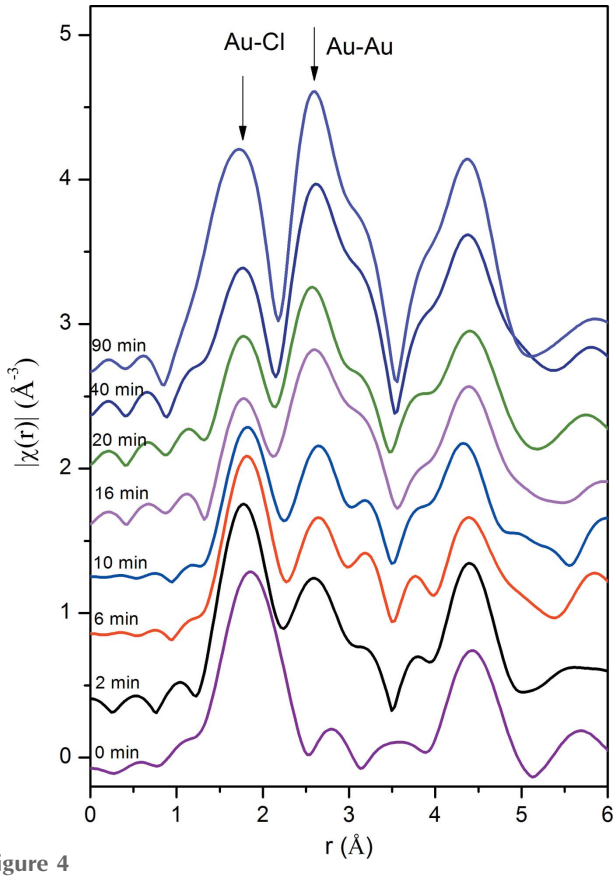

Figure 4
Fourier-transformed EXAFS spectra of Au nanoparticle precursor solution measured at the Au L_3-edge at different time intervals after mixing the reducers.

It can be observed that within 2 min a small peak appears corresponding to the Au—Au bond. The bond lengths of both Au—Cl and Au—Au bonds do not change significantly during the reaction. Fig. 6 shows the variation of coordination number of both bonds which shows that the Au—Au coordination remains near 5 until 10 min and subsequently increases and reaches the coordination of ~11 at about 70 min. The

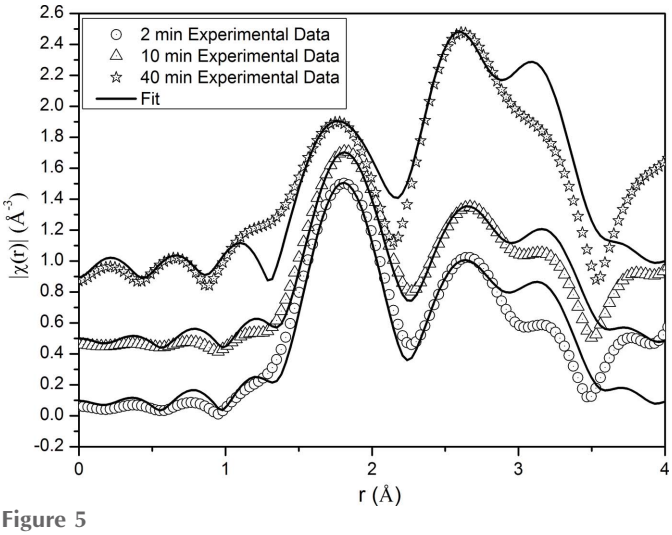

Figure 5
Plot of experimental FT-EXAFS data at the Au L_3-edge along with the best theoretical fit at different reaction times.

Au—Cl bond coordination, on the other hand, decreases until 20 min, after which it starts to increase again.

It should also be mentioned here that EXAFS cannot directly yield information on particle sizes and one way to overcome this problem is to carry out EXAFS and SAXS measurements simultaneously, as had been done by Polte *et al.* (2010). However, in that case SAXS measurements have to be carried out in transmission mode and EXAFS in fluorescence mode and there might be a possibility that the two techniques probe different sample volumes. In the present case we have carried out EXAFS and XANES both in transmission mode and obtained particle sizes from the coordination numbers determined from EXAFS analysis as described below (Frenkel *et al.*, 2011). Assuming the nanoparticles to be spherical, Calvin *et al.* (2003) devised a formula to correlate the coordination number and the particle size as:

$$n_{\rm nano} = \left[1 - \frac{3}{4}\left(\frac{r}{R}\right) + \frac{1}{16}\left(\frac{r}{R}\right)^3\right] n_{\rm bulk}, \qquad (4)$$

where r is the distance between the nearest neighbor atoms, R is the particle radius, $n_{\rm nano}$ is the coordination number for the nanoparticles and $n_{\rm bulk}$ is the bulk coordination number. Using the values of the Au—Au coordination numbers given in Fig. 6 as a function of time, particle sizes have been obtained for Au nanoparticles using equation (4) and are plotted as a function of time in Fig. 6. However, it should be noted here that the particle size determined by this method is based on the assumption that particles are spherical and hence gives good proximity to the final particle size as determined by TEM, but it fails to predict the cluster sizes formed during the initial stages of growth due to their non-spherical shapes.

Fig. 7 shows the visible absorbance spectra during the growth of gold nanoparticles. The absorbance increases with time and a peak appears between 520 nm and 540 nm which corresponds to the surface plasmon resonance (SPR) peak of the gold nanoparticles. The intensity of the SPR peak has been plotted in Fig. 8 as a function of time. The peak maximum also shifts from 527 nm to 540 nm during the initial phase of the reaction indicating the increase in particle size. The variation

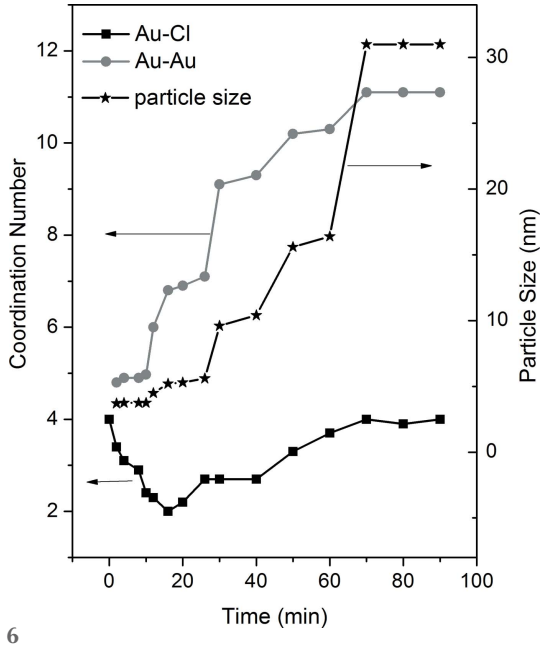

Figure 6
Variation of Au and Cl coordinations around Au sites and particle size obtained from EXAFS measurements on the Au precursor solution as a function of time measured from the instant of mixing the reducers.

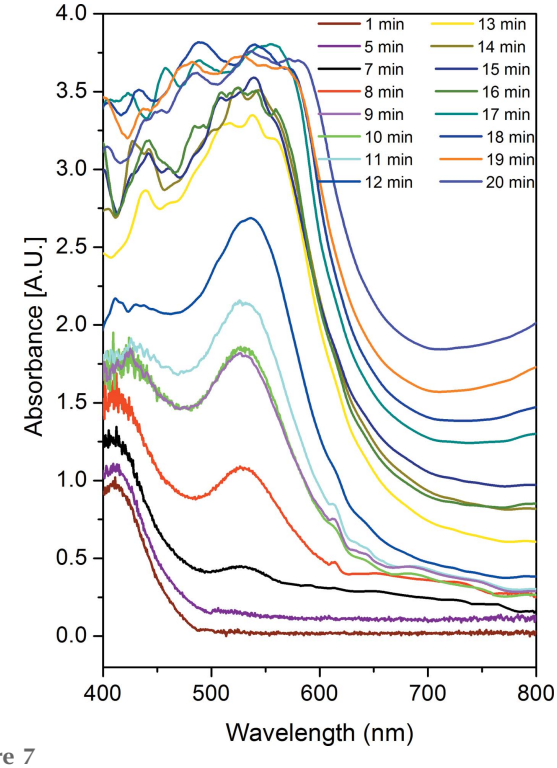

Figure 7
UV–Vis spectra of Au nanoparticle precursor solution measured in the wavelength range 400–800 nm at different time intervals after mixing the reducers.

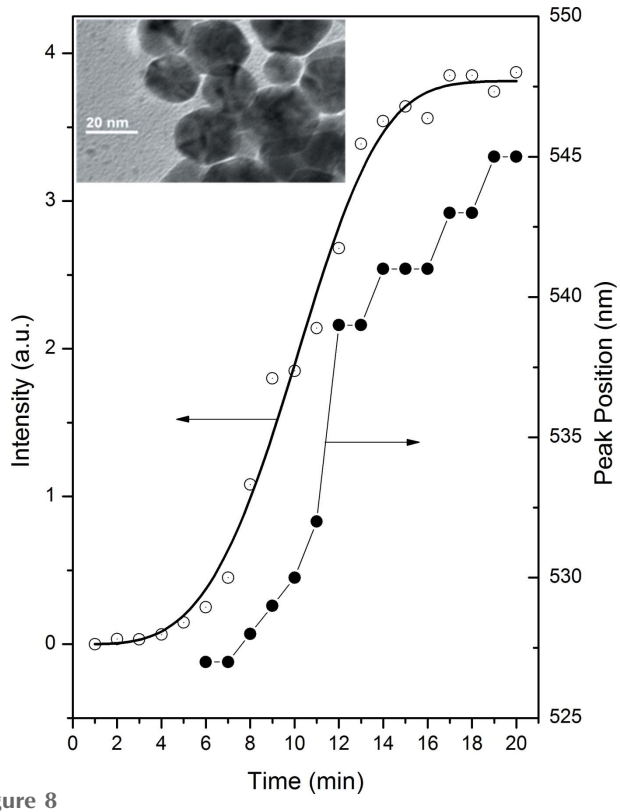

Figure 8
Variation of intensity and position of the Au surface plasmon peak in the UV–Vis spectra of Au precursor solution as a function of time measured from the instant of mixing the reducers. Inset: TEM micrograph of fully formed Au nanoparticles.

of peak position has also been plotted in Fig. 8 as a function of time. A TEM micrograph of gold nanoparticles formed by completely reducing $HAuCl_4$ by sodium citrate and P85 block copolymer is shown in the inset of Fig. 8. The figure shows that the Au nanoparticles formed are mostly spherical in shape and the size of most of the particles lies between 20 and 30 nm. This agrees with the final particle size obtained from EXAFS measurements as shown in Fig. 6.

As suggested by Sakai & Alexandridis (2005), the growth mechanism of block copolymer stabilized gold nanoparticles is governed by three main stages: (i) reduction of metal ions by block copolymer, (ii) absorption of block copolymer on gold clusters and reduction of metal ions on the surface, and (iii) growth of gold nanoparticles stabilized by block copolymer. In our case, as can be seen from Fig. 6, within 2 min of the start of the reaction Au clusters are formed. This provides evidence of fast reduction of the gold precursor and formation of a large number of nuclei which further grow into particles. The fast reduction of the precursor is also evident from the XANES spectra given in Fig. 3 and this phenomenon is similar to Lamers nucleation mechanism (Lamer & Dinegar, 1950) which suggests very fast nucleation and slow growth. In the next 10 min the Au—Au coordination remains the same at 4.9 while the Au—Cl bond breaks, which corresponds to the first stage of nucleation and growth discussed above. The Au—Au coordination of 4.9 is close to the average coordination number of three-dimensional Au clusters of 12 atoms with C_{2v} symmetry (Johansson *et al.*, 2008; Schooss *et al.*, 2010). These Au_{12} clusters act as seeds for further growth and, after 10 min, with the onset of the second stage, when the block copolymer is adsorbed on the surface of Au_{12} clusters, there is an increase of Au—Au coordination to 6.8 in the next 15 min which corresponds to the Au_{13} magic number of icosahedron clusters. Au_{13} clusters are highly stable as they fulfill the first geometrical shell closing. They exist in three preferred geometries, *i.e.* planar, cuboctahedral and icosahedral, with average coordination numbers of 4, 5.5 and 6.5, respectively. Theoretically the most stable Au_{13} structure is the planar; however, it has been found experimentally that the ligated Au_{13} icosahedron clusters are most stable due to ligand-induced charge transfer (Johansson *et al.*, 2008). After 25 min the coordination number again shows a jump from 7 to 9 which may correspond to the cuboctahedral Au_{147} clusters. Au_{147} clusters are also magic number clusters which show very high stability due to the closing of a third geometrical structure (Petkov *et al.*, 2008). After 30 min the Au nanoparticle growth starts and in 70 min it reaches the size of 31 nm with coordination approaching a bulk value of 12. Hence the third stage of the growth process is found to begin after 30 min from the start of the reaction and the stabilization of these nanoparticles occurs along with the growth process. Therefore, the growth of gold nanoparticles occurs through the formation of Au_{12} clusters which grow into Au_{13} icosahedron clusters and subsequently to cuboctahedral Au_{147} clusters which finally grow into spherical gold nanoparticles. It can also be seen from Fig. 6 that the first-shell coordination around the Au site does not decrease below 2 even though the XANES spectra show the presence of a mostly metallic Au state and after 20 min the Au—Cl bond coordination increases. Such a high value of coordination of the Au—Cl shell has also been observed by Ma *et al.* (2013) and Yao *et al.* (2010) during formation of Au nanoparticls by reduction of $HAuCl_4$, even after a sufficiently long time of the reduction reaction, and this phenomenon has been attributed to chloride capping of Au nanoparticles after formation.

The first two stages of the growth process as described above can also be corroborated by time-resolved UV–Vis spectroscopy studies. As can be seen from Fig. 8, the nature of the variation of the intensity of the surface plasmon peak up to 20 min of the growth process exactly follows the pattern of variation of the Au coordination number as shown in Fig. 6. The growth process cannot be probed further by UV–Vis spectroscopy since the absorption becomes too high for detection of the transmitted beam.

3.2. Growth of platinum nanoparticles

Fig. 9 shows the *in situ* time-resolved XANES spectra of the platinum nanoparticle precursor solution measured at the Pt L_3-edge. The near-edge spectrum of H_2PtCl_6 shows a white line at 11571 eV which is due to the electronic transition from the $2p_{3/2}$ to 5*d* state. This white line is a characteristic of Pt^{+4} ions and disappears for metallic Pt due to fully filled 5*d* states. The decrease in the intensity of the white line and finally its

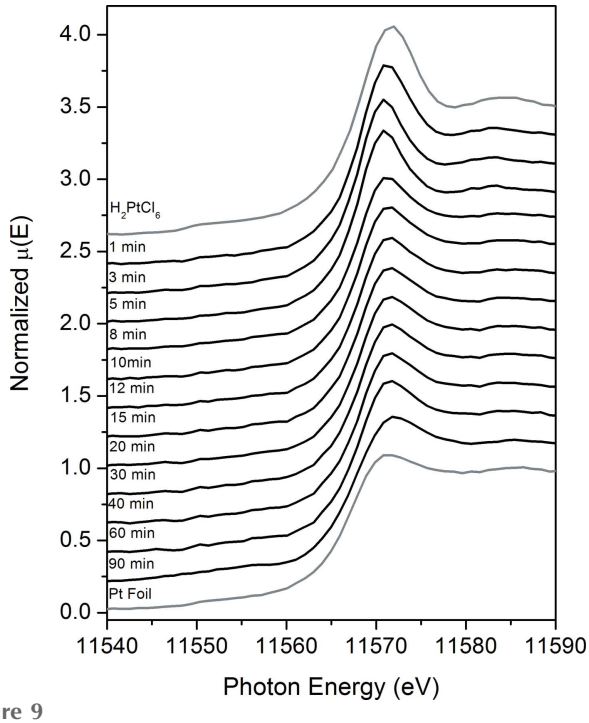

Figure 9
XANES spectra of Pt nanoparticle precursor solution measured at the Pt L_3-edge at different time intervals after mixing reducers.

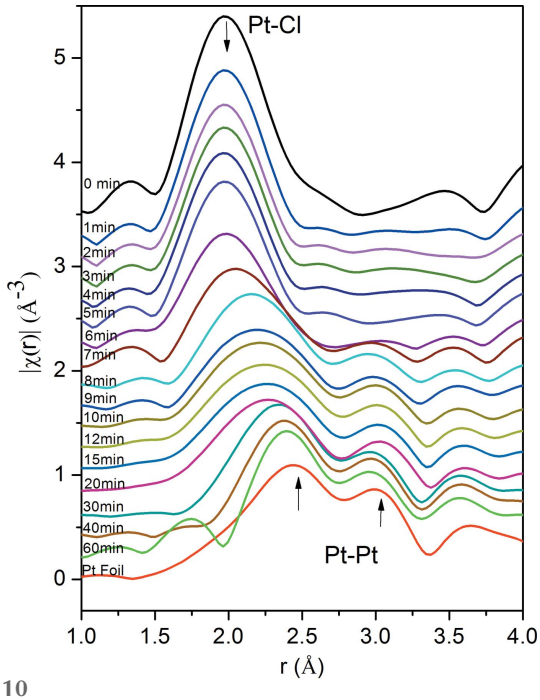

Figure 10
Fourier-transformed EXAFS spectra of Pt nanoparticle precursor solution measured at the Pt L_3-edge at different time intervals after mixing reducers.

disappearance with time suggests reduction of H_2PtCl_6 and formation of metallic platinum nanoparticles. After 90 min from the start of the reaction, the XANES spectrum completely resembles that of metallic platinum. A linear combination fit of the time-resolved XANES spectra was performed considering the spectra of H_2PtCl_6 and Pt foil as standards of the +4 and +0 states from which it has been observed that, in 6 min, 50% of the Pt cations are found to be in the metallic (+0) state and after 90 min ~82% of the Pt cations are reduced to the +0 state.

The $\chi(k)$ *versus* k spectra have been derived from the $\mu(E)$ *versus* E spectra following the steps described in the previous section. The $\chi(k)$ spectra are weighted by k^2 and the functions $\chi(k)k^2$ are Fourier transformed in the k range 2–10 Å^{-1} to generate the $\chi(r)$ *versus* r (or FT-EXAFS) spectra in terms of the real distances from the centre of the absorbing atom. Fig. 10 shows the $\chi(r)$ *versus* r spectra at different time intervals during the growth of platinum nanoparticles. The first peak (~1.8 Å) corresponds to the Pt—Cl bond and the second peak (~2.4 Å) corresponds to the Pt—Pt bond. The $\chi(r)$ *versus* r spectra have been fitted assuming a Pt—Cl path and a Pt—Pt path. The values of the Debye–Waller factors (σ^2) have been kept fixed at 0.005 and 0.004 for the Pt—Cl and Pt—Pt bond, respectively. The $R_{\rm factor}$ values for all the fittings are less than 0.01 which ensures a good fit of the data. The experimental $\chi(r)$ *versus* r data for some of the representative reaction times, along with their best-fit theoretical plots carried out as discussed above, have been shown in Fig. 11. The bond lengths of both Pt—Cl and Pt—Pt bonds do not change significantly during the reaction; however, the coordination numbers change with time and the variations of coordination number of both bonds are shown in Fig. 12. Using Calvin's approach (Calvin *et al.*, 2003), the sizes of the Pt nanoparticles have been obtained from the Pt—Pt coordination numbers through equation (4) and have also been plotted as a function of time in Fig. 12.

Fig. 13 shows the evolution of the UV–Vis absorbance spectra during the growth of platinum nanoparticles. The spectrum at 1 min shows two peaks at 328 nm and 394 nm due to $PtCl_6^{2-}$ whose intensity decreases with time in the first 5 min and, while the reaction proceeds further, the total absorbance increases. Fig. 14 shows the variation of the

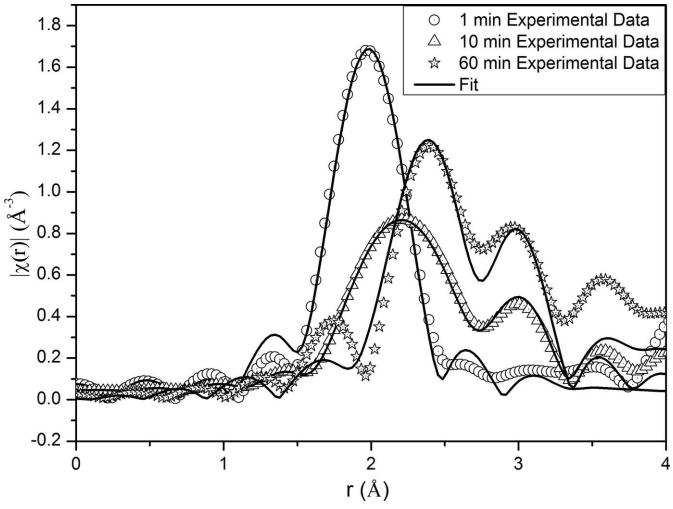

Figure 11
Plot of experimental FT-EXAFS data at the Pt L_3-edge along with the best theoretical fit at different reaction times.

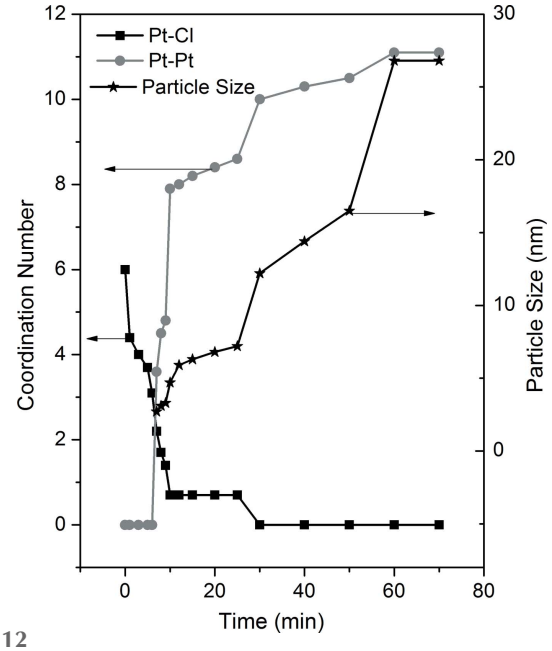

Figure 12
Variation of Pt and Cl coordinations around Pt sites and particle size obtained from EXAFS measurements on the Pt precursor solution as a function of time intervals measured from the instant of mixing the reducers.

intensity of absorbance at 324 nm, 394 nm and 450 nm with time. The increase in intensity at 450 nm wavelength manifests the growth of Pt nanoparticles. The inset of Fig. 14 shows the TEM image of Pt nanoparticles obtained from the solutions after 90 min of reaction which shows that the fully formed nanoparticles are mostly spherical in size with an average size

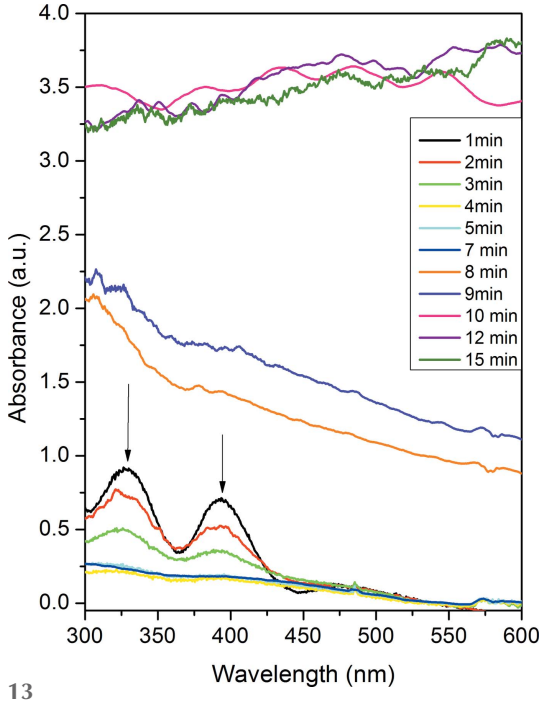

Figure 13
UV–Vis spectra of Pt nanoparticle precursor solution measured in the wavelength range 300–600 nm at different time intervals after mixing the reducers.

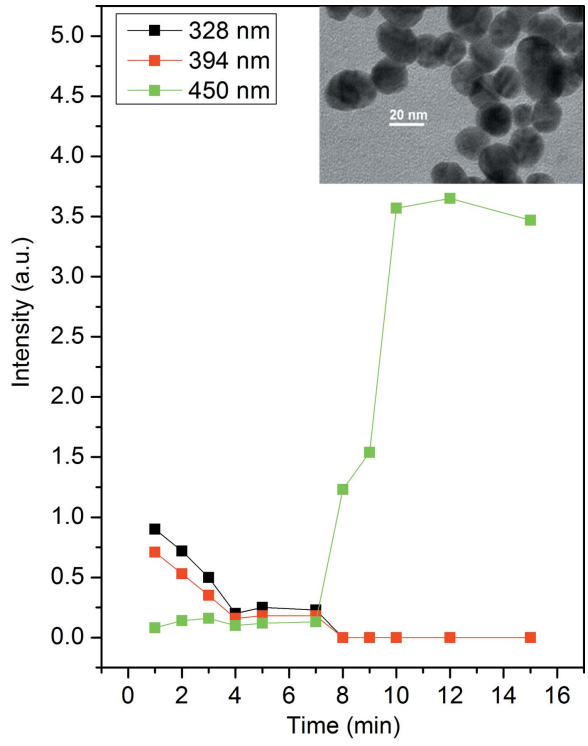

Figure 14
Variation of the intensity of absorption at 328, 394 and 450 nm in the UV–Vis spectra of Pt precursor solution as a function of time intervals measured from the instant of mixing the reducers. Inset: TEM micrograph of fully formed Pt nanoparticles.

of ∼20 nm, which agrees well with the final particle size obtained from EXAFS measurements as shown in Fig. 12.

The formation process of Pt nanoparticles can also be divided into three stages similar to that of gold nanoparticles. As can be seen from Fig. 12, the Pt—Cl bond breaks from the start of the reaction signifying the reduction of the precursor H_2PtCl_6. The Pt—Cl bond coordination suddenly drops from 6 to 4, after which it gradually decreases. This may indicate the reduction of $Pt^{IV}Cl_6^{2-}$ ions to $Pt^{II}Cl_4^{2-}$ ions. It has already been found that the $Pt^{IV}Cl_6^{2-}$ ions inhibit the formation of Pt nanoparticles (Harada & Kamigaito, 2012). Therefore, in the reduction process Pt^{+4} is first reduced to Pt^{+2} and then to Pt^{+0}. After 7 min a small peak appears in Fig. 10 along with an increase in Pt—Pt coordination in Fig. 12 showing the formation of the Pt—Pt bond. This sudden jump in Pt—Pt coordination corresponds to the phenomenon of Lamer's nucleation burst (Tromp *et al.*, 2003). This is similar to the growth of gold nanoparticles discussed in the earlier section. However, in the case of gold, Lamer nucleation occurs within 2 min from the start of the reaction, while platinum shows the nucleation burst at 7 min from the start. This difference may be due to the difference in the reduction potential of the two noble metal precursors, *i.e.* $Au^{III}Cl_4^-$ having a higher reduction potential than $Pt^{IV}Cl_6^{2-}$. From 7 to 9 min the Pt—Pt coordination remains around 4.5, indicating the formation of Pt_{12} clusters (Kumar & Kawazoe, 2008) which manifest the first stage of the reaction. The second stage starts at 10 min with a drastic increase in the Pt—Pt coordination to 7.9 which

possibly corresponds to formation of cuboctahedral Pt_{55} clusters. Pt_{55} is a magic cluster with the closing of a second geometrical shell. A cuboctahedron structure of 55 atoms has an average coordination number of 7.8, while the icosahedrons structure with 55 atoms have 8.5 as average coordination (Genest *et al.*, 2009). In the third stage, Pt—Pt coordination increases to its bulk value of 11 until 60 min through a slower process similar to the Au case. Therefore, during the growth of Pt nanoparticles, initially Pt_{12} clusters are formed which grow into cuboctahedral Pt_{55} clusters which further grow into spherical Pt nanoparticles. The formation of Pt_{55} clusters during the growth of Pt nanoparticles has also been reported by Harada & Kamigaito (2012). The first two stages of growth of the Pt nanoparticles can also be corroborated by UV–Vis spectroscopy, where, as can be seen from Fig. 14, the intensity at 450 nm grows similarly to the coordination number (Fig. 12) up to 10 min of reaction.

4. Conclusion

A setup has been developed at the energy-dispersive EXAFS beamline (BL-08) at INDUS-2 SRS at RRCAT, Indore, India, for *in situ* XAS measurements on chemical processes using a specially designed Teflon cell with one optical path for X-rays in the direction of the synchrotron beam and another in the perpendicular direction for visible radiation. Using the above setup the growth of Au and Pt nanoparticles from their respective chloride precursors using block copolymer-based reducers-cum-stabilizers has been studied by simultaneous *in situ* measurement of XAS and UV–Vis spectroscopy. The growth kinetics of both types of nanoparticles are found to be almost similar and are found to follow the three stages *viz.* (i) reduction of metal ions by block copolymer and formation of small cluster of typical five coordinations, (ii) absorption of block copolymer and reduction of metal ions on the surface of the cluster and increase in cluster size, and (iii) growth of gold nanoparticles stabilized by block copolymer. It can be observed that the time scale involved in the second and third stages of the nanoparticle formation are similar for both gold and platinum nanoparticles. This may be due to the fact that these stages are mainly governed by the block copolymer which is the same in both cases. This also consolidates the role of the block copolymer in the formation of these nanoparticles. However, the first stage of nucleation takes place earlier in the case of Au than in the case of Pt due to the difference in the reduction potential of the respective precursors. In both cases, 12 atoms clusters are formed which act as seeds for further growth. However, for gold, these 12 atoms clusters first grow into the magic number 13 atoms clusters and then 147 atoms clusters which further grow into gold nanoparticles. For platinum the 12 atoms clusters grow into the magic number 55 atoms clusters which further grow into platinum nanoparticles. The first two stages of the growth of Au and Pt nanoparticles as obtained by *in situ* XAS measurements are also corroborated by simultaneous *in situ* measurement of UV–Vis spectroscopy.

Acknowledgements

The authors wish to thank Dr A. Chakrabarti and Dr C. Kamal of ISUD, RRCAT, for their valuable suggestions in the course of this work. The help of Dr A. K. Shrivastava is also gratefully acknowledged for obtaining the TEM micrographs.

References

Abécassis, B., Testard, F., Spalla, O. & Barboux, P. (2007). *Nano Lett.* **7**, 1723–1727.
Bauer, M. & Gastl, C. (2010). *Phys. Chem. Chem. Phys.* **12**, 5575–5584.
Bauer, M., Heusel, G., Mangold, S. & Bertagnolli, H. (2010). *J. Synchrotron Rad.* **17**, 273–279.
Bhattacharyya, D., Poswal, A. K., Jha, S. N., Sangeeta & Sabharwal, S. C. (2009). *Nucl. Instrum. Methods Phys. Res. A*, **609**, 286–293.
Boita, J., Nicolao, L., Alves, M. C. M. & Morais, J. (2014). *Phys. Chem. Chem. Phys.* **16**, 17640–17647.
Bond, G. C., Louise, C. & Thompson, D. T. (2006). *Catalysis by Gold*, Vol. 6. London: Imperial College Press.
Briois, V., Lützenkirchen-Hecht, D., Villain, F., Fonda, E., Belin, S., Griesebock, B. & Frahm, R. (2005). *J. Phys. Chem. A*, **109**, 320–329.
Caetano, B. L., Santilli, C. V., Meneau, F., Briois, V. & Pulcinelli, S. H. (2011). *J. Phys. Chem. C*, **115**, 4404–4412.
Calvin, S., Miller, M. M., Goswami, R., Cheng, S. F., Mulvaney, S. P., Whitman, L. J. & Harris, V. J. (2003). *J. Appl. Phys.* **94**, 778–783.
Das, N. C., Jha, S. N., Bhattacharyya, D., Poswal, A. K., Sinha, A. K. & Mishra, V. K. (2004). *Sadhana*, **29**, 545–558.
Frenkel, A. I., Yevick, A., Cooper, C. & Vasic, R. (2011). *Annu. Rev. Anal. Chem.* **4**, 23–39.
Genest, A., Krüger, S. & Rösch, N. (2009). *Z. Naturforsch. B*, **64**, 1246–1258.
Harada, M. & Kamigaito, Y. (2012). *Langmuir*, **28**, 2415–2428.
Helmbrecht, C., Hecht, D. L. & Frank, W. (2015). *Nanoscale*, **7**, 4978–4983.
Hu, Z. S., Escamilla Ramírez, D. J., Heredia Cervera, B. E., Oskam, G. & Searson, P. C. (2005). *J. Phys. Chem. B*, **109**, 11209–11214.
Johansson, M. P., Lechtken, A., Schooss, D., Kappes, M. M. & Furche, F. (2008). *Phys. Rev. A*, **77**, 053202.
Konigsberger, D. C. & Prins, R. (1988). *X-ray Absorption: Principles, Applications, Techniques of EXAFS, SEXAFS and XANES*. New York: Wiley.
Kumar, V. & Kawazoe, Y. (2008). *Phys. Rev. B*, **77**, 205418.
LaMer, V. K. & Dinegar, R. H. (1950). *J. Am. Chem. Soc.* **72**, 4847–4854.
Lin, C. S., Khan, M. R. & Lin, S. D. (2006). *J. Colloid Interface Sci.* **299**, 678–685.
Louis, C. & Pluchery, O. (2012). *Gold Nanoparticles for Physics, Chemistry and Biology*. London: Imperial College Press.
Ma, J., Zou, Y., Jiang, Z., Huang, W., Li, J., Wu, G., Huang, Y. & Xu, H. (2013). *Phys. Chem. Chem. Phys.* **15**, 11904–11908.
Menard, L. D., Xu, H., Gao, S. P., Twesten, R. D., Harper, A. S., Song, Y., Wang, G., Douglas, A. D., Yang, J. C., Frenkel, A. I., Murray, R. W. & Nuzzo, R. G. (2006). *J. Phys. Chem. B*, **110**, 14564–14573.
Narayanan, R. & El-Sayed, M. A. (2004). *J. Am. Chem. Soc.* **126**, 7194–7195.
Newton, M. A., Jyoti, B., Dent, A. J., Fiddy, S. G. & Evans, J. (2004). *Chem. Commun.* **21**, 2382.
Newville, M. (2001). *J. Synchrotron Rad.* **8**, 322–324.
Ohyama, J., Teramura, K., Higuchi, Y., Shishido, T., Hitomi, Y., Kato, K., Tanida, H., Uruga, T. & Tanaka, T. (2011). *Chem. Phys. Chem.* **12**, 127–131.
Petkov, V., Bedford, N., Knecht, M. R., Weir, M. G., Crooks, R. M., Tang, W., Henkelman, G. & Frenkel, A. (2008). *J. Phys. Chem. C*, **112**, 8907–8911.

Polte, J., Ahner, T. T., Delissen, F., Sokolov, S., Emmerling, F., Thünemann, A. F. & Kraehnert, R. (2010). *J. Am. Chem. Soc.* **132**, 1296–1301.
Ray, D., Aswal, V. K. & Kohlbrecher, J. (2011). *Langmuir*, **27**, 4048–4056.
Sakai, T. & Alexandridis, P. (2005). *J. Phys. Chem. B*, **109**, 7766–7777.
Schmid, G. (2006). *Nanoparticles: From Theory to Application.* New York: Wiley.
Schooss, D., Weis, P., Hampe, O. & Kappes, M. M. (2010). *Philos. Trans. R. Soc. A*, **368**, 1211–1243.
Shannon, I. J., Maschmeyer, T., Sankar, G., Thomas, J. M., Oldroyd, R. D., Sheehy, M., Madill, D., Waller, A. M. & Townsend, R. P. (1997). *Catal. Lett.* **44**, 23–27.
Simonsen, S. B., Chorkendorff, I., Dahl, S., Skoglundh, M., Sehested, J. & Helveg, S. J. (2010). *J. Am. Chem. Soc.* **132**, 7968–7975.
Storhoff, J. J., Elghanian, R., Mucic, R. C., Mirkin, C. A. & Letsinger, R. L. (1998). *J. Am. Chem. Soc.* **120**, 1959–1964.
Tromp, M., Sietsma, J. R. A., van Bokhoven, J. A., van Strijdonck, G. P. F., van Haaren, R. J., van der Eerden, A. M. J., van Leeuwen, P. W. N. M. & Koningsberger, D. C. (2003). *Chem. Commun.* **2003**, 128–129.
Tsung, C. K., Kuhn, J. N., Huang, W., Aliaga, C., Hung, L. I., Somorjai, G. A. & Yang, P. J. (2009). *J. Am. Chem. Soc.* **131**, 5816–5822.
Tsunoyama, H., Ichikuni, N., Sakurai, H. & Tsukuda, T. (2009). *J. Am. Chem. Soc.* **131**, 7086–7093.
Wang, Q., Hanson, J. C. & Frenkel, A. I. (2008). *J. Chem. Phys.* **129**, 234502.
Wong, E. M., Bonevich, J. E. & Searson, P. C. (1998). *J. Phys. Chem. B*, **102**, 7770–7775.
Yao, S., Yuan, Y., Xiao, C., Li, W., Kou, Y., Dyson, P. J., Yan, N., Asakura, H., Teramura, K. & Tanaka, T. (2012). *J. Phys. Chem. C*, **116**, 15076–15086.
Yao, T., Sun, Z., Li, Y., Pan, Z., Wei, H., Xie, Y., Nomura, M., Niwa, Y., Yan, W., Wu, Z., Jiang, Y., Liu, Q. & Wei, S. (2010). *J. Am. Chem. Soc.* **132**, 7696–7701.
Zheng, H., Smith, R. K., Jun, Y.-W., Kisielowski, C., Dahmen, U. & Alivisatos, A. P. (2009). *Science*, **324**, 1309–1312.